



Phosphorus Cycle and Primary Productivity Changes in the Tethys Ocean During the Permian-Triassic Transition: Starving Marine Ecosystems

Johann Müller^{1*}, Yadong Sun^{1*}, Fen Yang², Alicia Fantasia³ and Michael Joachimski¹

¹GeoZentrum Nordbayern, Friedrich-Alexander University Erlangen-Nürnberg (FAU), Erlangen, Germany, ²State Key Laboratory of Biogeology and Environmental Geology, China University of Geosciences, Wuhan, China, ³University Lyon, UCBL, ENSL, UJM, CNRS, LGL-TPE, Villeurbanne, France

OPEN ACCESS

Edited by:

Sara Callegaro,
University of Oslo, Norway

Reviewed by:

Stephen Grasby,
Geological Survey of Canada, Canada
William J. Foster,
University of Hamburg, Germany

*Correspondence:

Johann Müller
johann.jm.mueller@fau.de
Yadong Sun
yadong.sun@fau.de

Specialty section:

This article was submitted to
Biogeoscience,
a section of the journal
Frontiers in Earth Science

Received: 09 December 2021

Accepted: 10 February 2022

Published: 09 March 2022

Citation:

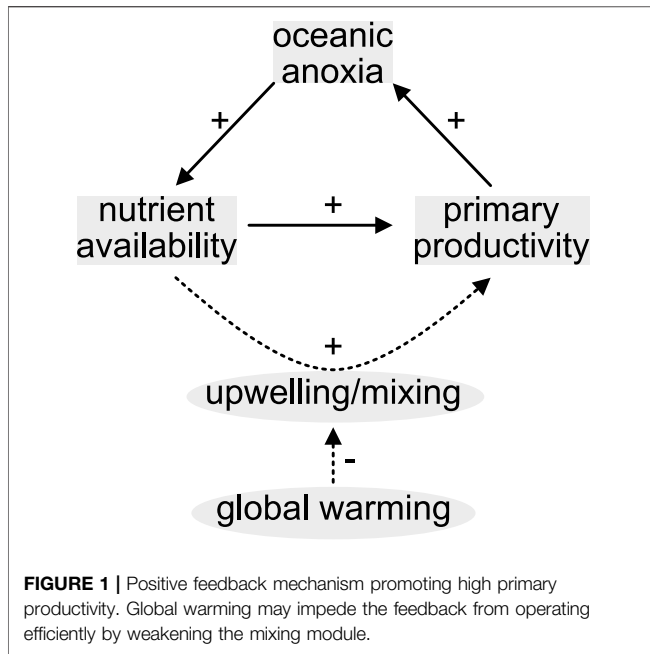
Müller J, Sun Y, Yang F, Fantasia A and
Joachimski M (2022) Phosphorus
Cycle and Primary Productivity
Changes in the Tethys Ocean During
the Permian-Triassic Transition:
Starving Marine Ecosystems.
Front. Earth Sci. 10:832308.
doi: 10.3389/feart.2022.832308

The ultimate cause(s) of the end-Permian mass extinction (~252 Ma ago) has been disputed. A complex interplay of various effects, rather than a single, universal killing mechanism, were most likely involved. Climate warming as consequence of greenhouse gas emissions by contemporaneous Siberian Traps volcanism is widely accepted as an initial trigger. Synergetic effects of global warming include increasing stratification of the oceans, inefficient water column mixing, and eventually low marine primary productivity culminating in a series of consequences for higher trophic levels. To explore this scenario in the context of the end-Permian mass extinction, we investigated sedimentary total organic carbon, phosphorus speciation as well as nickel concentrations in two low-latitude Tethyan carbonate sections spanning the Permian-Triassic transition. Total organic carbon, reactive phosphorus and nickel concentrations all decrease in the latest Permian and are low during the Early Triassic, pointing to a decline in primary productivity within the Tethyan realm. We suggest that the productivity collapse started in the upper *C. yini* conodont Zone, approximately 30 ka prior to the main marine extinction interval. Reduced primary productivity would have resulted in food shortage and thus may serve as explanation for pre-mass extinction perturbations among marine heterotrophic organisms.

Keywords: phosphorus cycle, primary productivity, nutrients, food shortage, Permian-Triassic, end-Permian mass extinction, phosphorus speciation

INTRODUCTION

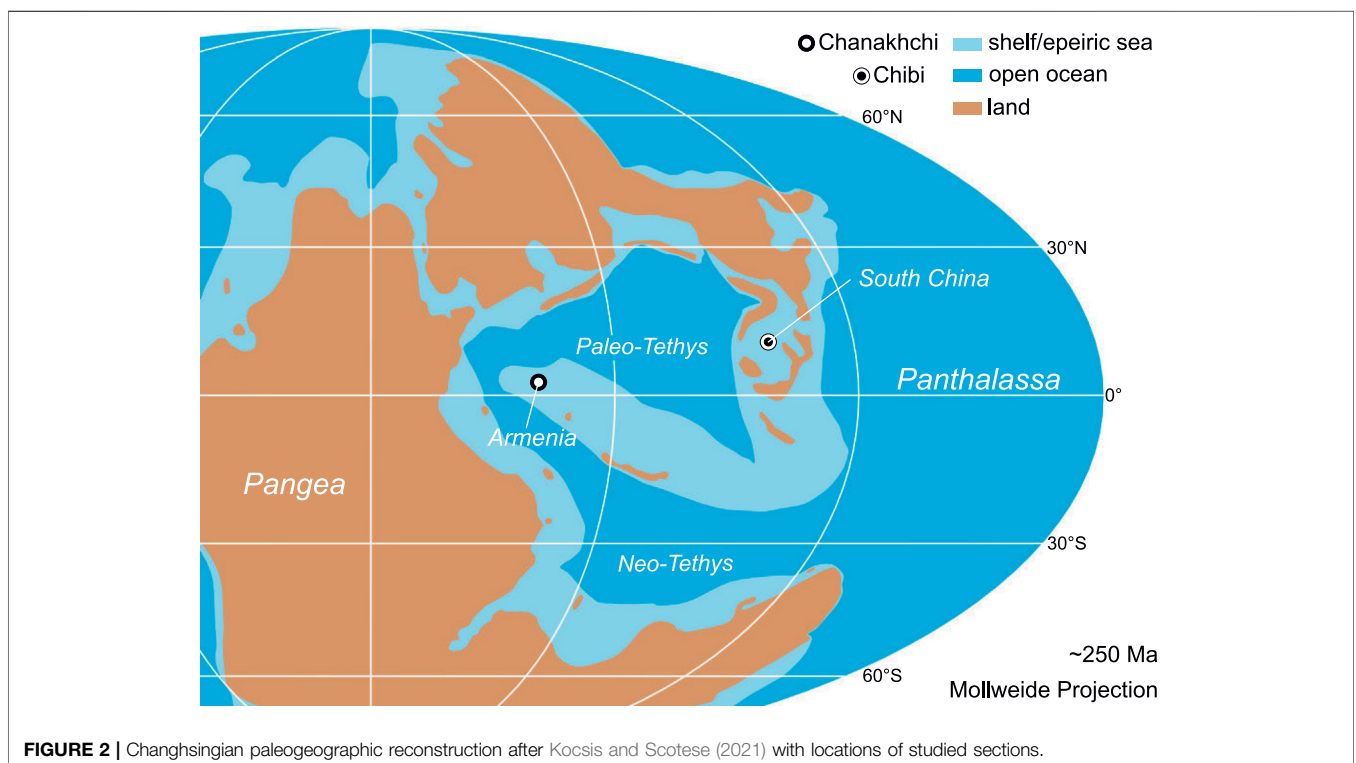
Anthropogenic global warming is expected to decline marine primary productivity with severe consequences for global ecosystems as well as for mankind (Mora et al., 2013). This is because climate warming likely slows down the meridional overturning circulation, decreases wind-driven coastal and equatorial upwelling intensity but increases thermal stratification thereby inhibiting the mixing of shallow and deep waters (Behrenfeld et al., 2006). Bulk primary production in today's oceans is mainly confined to equatorial and shelf areas where upwelling systems replenish nutrients to the euphotic zone (Boyd et al., 2014). In general, there is a complex interplay between water column mixing, oxygen saturation of sea water, nutrient levels



in the euphotic zone, primary productivity, and organic carbon export to deep waters and the sediment. For example, 1) upwelling systems replenish phosphorus (P) to the euphotic zone 2) organic matter remineralization consumes oxygen and 3) seafloor hypoxia favors P recycling from sediments (**Figure 1**; e.g., Ingall et al., 1993). Under normal climatic conditions, this eutrophication feedback mechanism is able to

maintain high levels of productivity in coastal shelf areas, e.g., in the euphotic zone along the modern Peruvian margin (Burnett et al., 1982). However, if vertical mixing weakens due to warming, the nutrient P will be trapped in deeper waters where it cannot be utilized by phytoplankton (Behrenfeld et al., 2006), ultimately leading to a food shortage for higher trophic levels.

To better understand the marine nutrient cycling in the context of ongoing global warming, it is of prime importance to investigate intervals of potent warming in the geological past. Among the so called “big five” mass extinctions, the end-Permian mass extinction stands out being regarded as the most devastating in the Phanerozoic (Newell, 1967; Raup and Sepkoski, 1982; Bambach et al., 2004; Stanley, 2016; Bond and Grasby, 2017). Several coinciding ecological changes were inferred from the geological record using different sedimentological, paleontological, and geochemical methods and many controversial hypotheses exist concerning their causal relationships with no consensus having been reached hitherto. For example, stable oxygen isotope studies of conodont apatite indicate that the Earth has experienced significant and relatively rapid global warming during the latest Permian (e.g., Joachimski et al., 2012; Sun et al., 2012; Schobben et al., 2014; Chen et al., 2020; Joachimski et al., 2020). Low latitude sea surface temperatures increased by $\sim 10^{\circ}\text{C}$ within ~ 40 ka from the latest Changhsingian into the Induan. The contemporaneity of Siberian Traps volcanism suggests that volcanogenic greenhouse gas emissions raised atmospheric $p\text{CO}_2$ to high levels (Svensen et al., 2009; Burgess et al., 2017). Additionally, the injection of isotopically light, volcanogenic carbon to the atmosphere



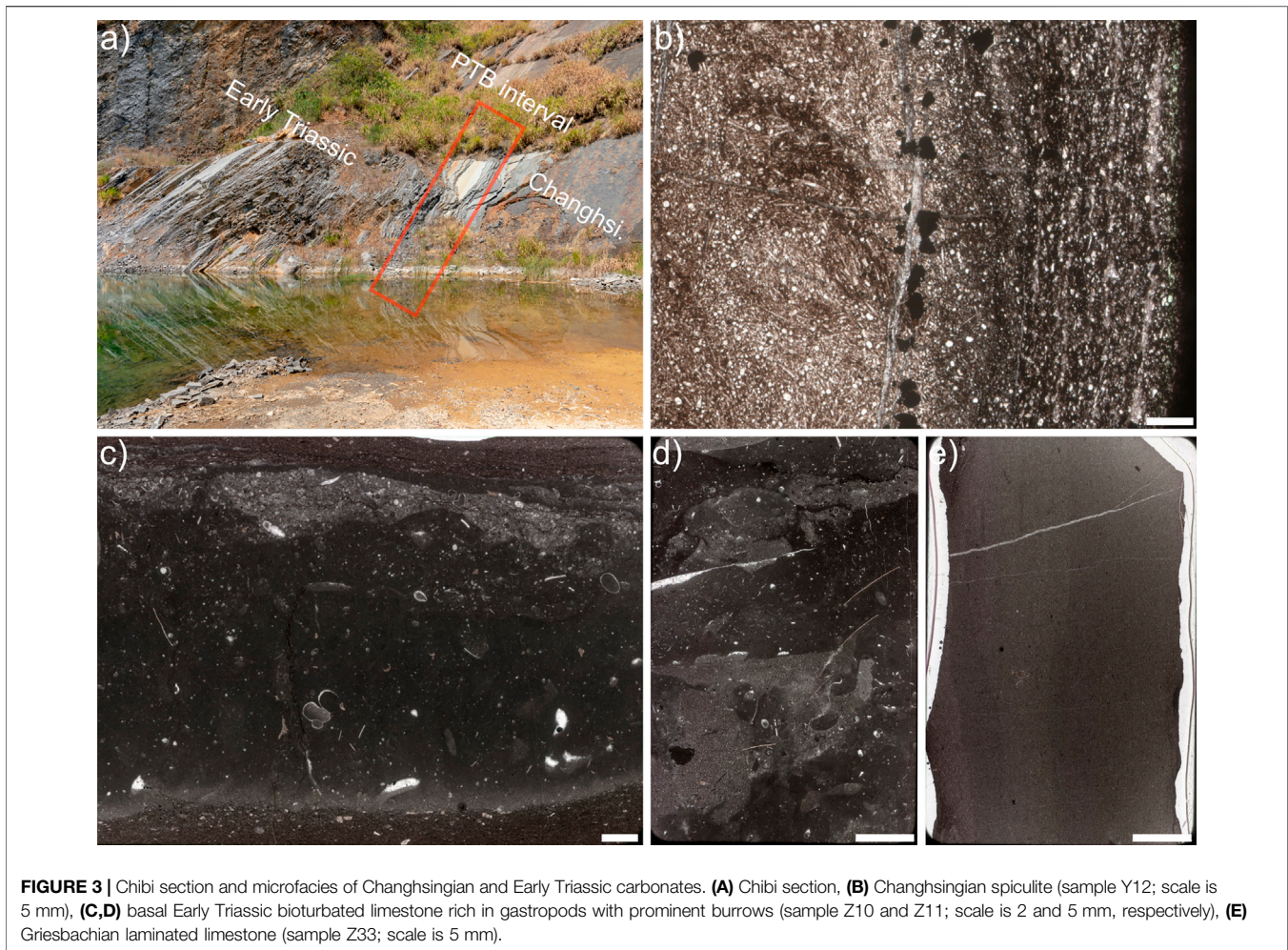


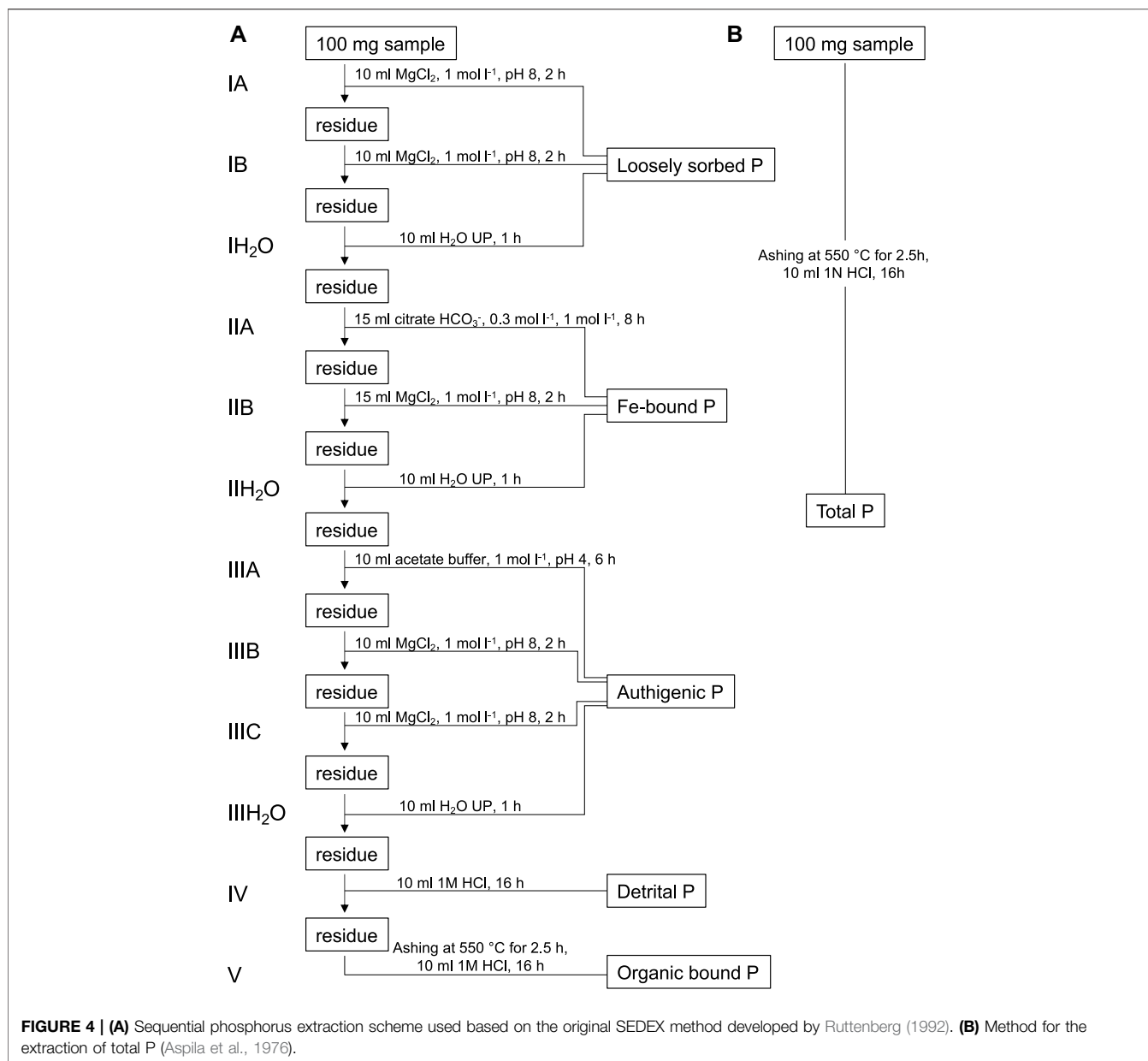
FIGURE 3 | Chibi section and microfacies of Changhsingian and Early Triassic carbonates. **(A)** Chibi section, **(B)** Changhsingian spiculite (sample Y12; scale is 5 mm), **(C,D)** basal Early Triassic bioturbated limestone rich in gastropods with prominent burrows (sample Z10 and Z11; scale is 2 and 5 mm, respectively), **(E)** Griesbachian laminated limestone (sample Z33; scale is 5 mm).

potentially generated the prominent negative carbon isotope excursion at the Permian-Triassic (P-T) boundary (Korte et al., 2010; Korte and Kozur, 2010; Shen et al., 2012). Intense ocean anoxia during the crisis interval was recognized early based on the widespread occurrence of sedimentary facies typical for deposition under hypoxic conditions (Wignall and Hallam, 1992; Wignall and Twitchett, 1996; Isozaki, 1997). This was confirmed by various proxies such as framboidal pyrite analysis, trace metal concentrations, stable sulfur and uranium isotopes and iron speciation further refining the record of P-T ocean anoxia (e.g., Riccardi et al., 2006; Grasby et al., 2013; Clarkson et al., 2016; Lau et al., 2016; Wignall et al., 2020). In contrast to the previously proposed P-T superanoxia, the current understanding is that of a spatially and temporally heterogeneous anoxic event that initiated ~70 ka prior to the main marine extinction level (Zhang et al., 2018).

While climate warming and ocean anoxia are reasonably well-established for the end-Permian mass extinction, marine primary productivity levels at the time remain intensively debated. Studies arguing for a boost in marine primary productivity through enhanced continental input of nutrients (i.e., eutrophication; e.g., Algeo and Twitchett, 2010; Schobben et al., 2020) are opposed to studies pointing

towards a productivity collapse due to strong ocean stratification and/or weak upwelling with inefficient nutrient shuttling to the euphotic zone (i.e., oligotrophication; e.g., Schoepfer et al., 2012; Grasby et al., 2016; Sun et al., 2021). Other authors point out that a loss of nitrate under anoxic conditions more likely resulted in an ammonium ocean during the end-Permian mass extinction and P was possibly not the limiting nutrient at the time (Sun et al., 2019; Grasby et al., 2020). The oligotrophication scenario is in better accordance with modelling results for the near future and changes we have already observed in the recent past (e.g., Bopp et al., 2013; Roxy et al., 2016). Furthermore, Earth system modelling for the P-T interval predicts a decline in net primary productivity (~40% globally) especially in low latitudes and a large P reservoir in the deep water column (Supplementary Figure S4 in Penn et al., 2018).

In order to document marine P cycling and associated changes of primary productivity in the Tethys Ocean during the critical P-T boundary interval, we investigated sedimentary P distributions, total organic carbon (TOC) and nickel (Ni) concentrations in two carbonate successions from South China and Armenia (Figure 2). A sequential P extraction method was applied to reconstruct bioavailable, reactive P (P_{react}). C/P molar



ratios are used to evaluate early diagenetic P transfer processes (sink switching) as well as the degree of P burial versus benthic P release (i.e., the P burial efficiency). The geochemical records from both studied sections suggest a decrease in primary productivity in the Tethyan region starting well before the end-Permian mass extinction.

MATERIALS AND METHODS

Geological Setting

Studied P-T boundary successions were deposited across the Paleotethys ocean at tropical latitudes between 0 and 20°N

(Kocsis and Scotese, 2021; **Figure 2**). The studied Chibi Section (29.7515 N, 113.9519 E) is located in South China about 100 km south of the city of Wuhan (Hubei Province). The study area is part of the South China Block which was situated in tropical latitudes at the eastern margin of the Paleotethys Ocean during the Lopingian. At that time, the South China Block was characterized by a vast carbonate platform (Yangtze Platform) passing into a deeper basin with siliceous carbonate and chert deposition further north. During the Wuchiapingian, the Chibi section was located on a shallow water platform, but as consequence of a relative sea level rise, the depositional setting changed to a deeper slope setting in the latest Changhsingian. The continuous sedimentary succession is

represented by the Lopingian Wujiaping and Dalong Formations as well as the Early Triassic Daye Formation. With the depositional environment deepening during the Changhsingian, dark gray to black siliceous carbonates and cherts with sponge spicules and radiolarian tests (Dalong Formation) were deposited. The P-T transition is characterized by a volcanic ash bed followed by thinly bedded, in part dolomitic light gray carbonates and marls of the Early Triassic (Daye Formation). While some latest Permian and Early Triassic beds are rich in gastropods and show signs of bioturbation, most carbonates are laminated and lack fossils (**Figure 3**).

The Chanakhchi (former Sovetashen) section (39.8412 N, 45.0491 E) is located in Central Armenia close to the village of Zangakaton about 60 km southeast of the capital Yerevan. The area is part of the South Armenian Block belonging to the Anatolide-Tauride South Armenian microplate, which rifted northward from North Gondwana in the late Paleozoic (Meijers et al., 2015). During the P-T transition, the Cimmerian terranes were located at tropical latitudes and separated the opening Neo-Tethys to the south from the closing Paleo-Tethys to the north. The Changhsingian is characterized by irregularly bedded to nodular gray to reddish limestones (Paratirolites Beds) followed by thin reddish marls with thin lenticular limestone beds (“Boundary Clay”) of the Akhura Formation. The latest Permian and basal Early Triassic are characterized by microbialites interfingering with reddish to gray micritic limestones. These are overlain by the Karabaglyar Formation, a monotonous succession of platy, non-bioturbated and partially laminated limestones of Griesbachian to Dienerian age. The prominent Early Triassic sponge microbial buildups suggest a platform environment between fair-weather and storm wave base during the earliest Triassic (Baud et al., 2007; Friesenbichler et al., 2018; Foster et al., 2020).

Samples

The sampling of the Chibi section started at the boundary between the Lopingian Wujiaping and Dalong Formations and reaches up a few meters into the Early Triassic Daye Formation (~14 m; **Figure 3**). Only fresh and unweathered hand specimens were collected bed by bed. One part of the samples was sent for thin section preparation while the other part was powdered for geochemical analyses. For the latter, weathered or altered surfaces as well as parts of the samples comprising diagenetic features like calcite veins were removed with a rock saw. After this, samples were crushed with a jaw crusher and ground to powder using an agate disc mill. Finally, powders were sieved passing through 125 µm and stored in polypropylene beakers.

Armenian samples were selected from an existing sample set taken in the Chanakhchi section during earlier field campaigns in 2011 and 2013 (Joachimski et al., 2020). The sampled interval covers the Lopingian Akhura Formation and the lower member of the Early Triassic Karabaglyar Formation (~44 m). Because samples were taken at a very high resolution, around 300 specimens were available. For this study 66 samples were selected in even intervals. Samples were put in a polypropylene sleeve and then crushed with a hammer. From the resulting rock chips fresh and unaltered rock pieces were

picked manually. Selected rock chips were powdered with an agate ball mill. To ensure that no coarse grains remained within the powder, samples were sieved through 125 µm and stored in polypropylene beakers.

Stable Carbon Isotope Analyses

Carbonate powders of samples from the Chibi section were reacted with phosphoric acid at 70°C using a Gasbench II connected to a ThermoFisher Delta V Plus isotope ratio mass spectrometer (IRMS) at the GZM Erlangen. Reproducibility and accuracy were monitored by replicate analysis of in-house standards calibrated against NBS19 (1.95‰) and LSVEC (-46.6‰). Reproducibility for δ¹³C was ±0.03‰ (1σ; n = 18). All values are reported in per mil ‰ using the standard delta notation (δ¹³C) relative to Vienna—Pee Dee Belemnite (V-PDB).

Quantification of Total Organic Carbon

For the determination of TOC contents, carbonate was removed by treating bulk rock powders with hydrochloric acid. About 5 g of each powdered sample were weighed into 250 ml glass beakers and approximately 200 ml of 10% HCl was added while carefully stirring with a glass rod. The beakers were then covered with a watch glass and placed on a hotplate at 50°C for a minimum of 12 h. The procedure was repeated in case there was still reaction observable after this time. Insoluble and carbonate free residues were repeatedly washed with deionized H₂O until the supernatant had a pH between 6 and 7. The insoluble residues were then transferred into pre-weighed evaporating dishes which were then placed into an oven at 50°C until they were dry and weights were constant. At last, the dry residues were homogenized with an agate pestle and mortar and stored in glass vials.

The organic carbon concentration of the insoluble residues was measured with a ThermoFisher Flash 2000 elemental analyzer connected to a Delta V Plus IRMS at the GZM Erlangen. Precision determined from replicate analyses of laboratory standards OAS (1.61% C) and Jon1 (0.44% C) was ±0.09% (1σ, n = 23) and ±0.05% (1σ, n = 5), respectively.

The TOC content of the original sample (TOC_{sample}) in % was calculated by multiplying the organic carbon concentration of the insoluble residues (OC_{res}) in % with the ratio between the weight of the insoluble residues (m_{res}) and the original samples (m_{sample}):

$$TOC_{sample} = OC_{res} \cdot \frac{m_{res}}{m_{sample}} \quad (1)$$

Sequential Phosphorus Extraction

In order to determine the concentration of bio-available or reactive P (P_{react}), we used the sequential phosphorus extraction method (SEDEX) developed by Ruttenberg (1992). The SEDEX technique enables to extract loosely adsorbed phosphorus (P_{ex}), P bound to Fe-oxyhydroxides (P_{Fe}), authigenic apatite-P (P_{auth}), detrital apatite-P (P_{det}), and P bound to organic matter (P_{org}) by treating sample powders with reagents of increasing “aggressivity” in five steps

TABLE 1 | Mean P concentrations in ppm of the different P species in replicate analyses of internal standard X1 ($n = 8$). 1σ - standard deviation, CV - coefficient of variation.

$n = 8$	Step I (sorbed)	Step III (authigenic)	Step IV (detrital)	Step V (organic)	P_{tot} (total)	P_{react} (reactive)
Mean	12.1	885.1	47.9	11.4	931.8	883.8
1σ	± 9	± 36	± 17	± 2	± 46	± 56
CV	73%	4%	36%	20%	5%	6%

(Figure 4). To avoid contamination only *p.a.* grade reagents and ultrapure (UP) H_2O (Merk MilliQ) were used. Additionally, all used glassware was cleaned in a 10% HCl bath for a minimum of 24 h and then rinsed three times with UP H_2O .

First, sample splits of about 100 mg were weighed into clean 50 ml polypropylene centrifuge tubes. To extract the P_{ex} fraction, the samples were treated with 10 ml MgCl_2 solution (1 mol L^{-1} , pH 8) twice for 2 h followed by a rinsing step with 10 ml UP H_2O for 1 h. After this, 15 ml of a citrate-bicarbonate solution (0.3 mol L^{-1} , 1 mol L^{-1} , pH 7.6) and 0.375 g sodium dithionite were added and centrifuge tubes were shaken for 8 h to extract P_{Fe} . Subsequently the residues were rinsed with 15 ml MgCl_2 solution for 2 h and with 10 ml UP H_2O for 1 h. This was followed by the extraction of P_{auth} using 10 ml of a sodium acetate buffer solution (1 mol L^{-1} , pH 4) for 6 h. Next, samples were rinsed with 10 ml MgCl_2 for 2 h and 10 ml UP H_2O for 1 h. After this, P_{det} was extracted from the residue by treating the residue with 1 M HCl for 16 h. Finally, the residues were transferred from the centrifuge tubes into glass vials and evaporated at 80°C in an oven. Once dry, 0.4 ml MgNO_3 solution (50% w v^{-1}) was added and the vials were placed in a furnace at 550°C for 2.5 h. Eventually, the ashed residues were treated with 10 ml 1 M HCl for another 16 h to extract P_{org} . To determine total P (P_{tot}) 0.4 ml MgNO_3 solution (50% w v^{-1}) was added to 100 mg sample splits in glass vials. Vials were placed in a furnace and samples were ashed for 2.5 h at 550°C . Residues were then treated with 1 M HCl for 16 h to extract P_{tot} (Aspila et al., 1976). It should be noted here that the P-fractions of the different steps are operationally defined and do not necessarily represent chemically discriminable entities.

To ensure that samples were in contact with the reagents throughout the procedure the powders must be kept suspended. This was accomplished by placing the centrifuge tubes onto a shaker table at a suitable speed. After each step the tubes were centrifuged at $4,000 \times g$ for 10 min and the supernatant solutions were decanted and filtered through $0.45 \mu\text{m}$ nylon syringe filters into clean 20 ml polyethylene bottles. The supernatants were then acidified with concentrated HCl and stored in a fridge until analysis.

Photometric Analyses

Concentrations of phosphate in the solutions generated by the SEDEX method (steps I, III, IV and V) were determined with the photometric ascorbic acid method developed by Murphy and Riley (1962). This method is based on the formation of a blue colored molybdate complex with the intensity of the blue color

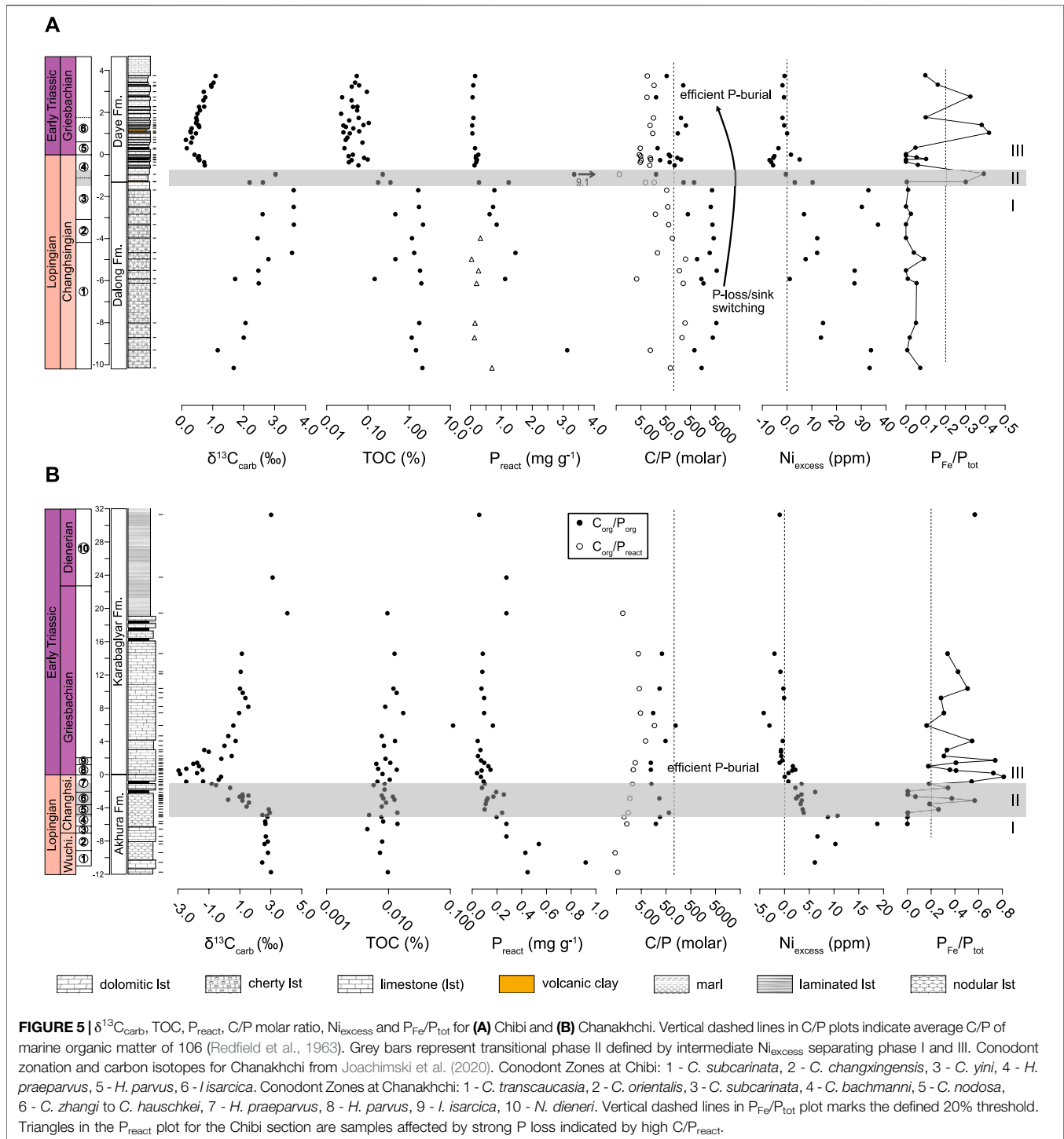
being proportional to the phosphate concentration in the solution.

For this, 100 μL of a mixing reagent (4.5 N sulfuric acid, 0.001 mol L^{-1} antimony potassium tartrate, 0.01 mol L^{-1} ammonium heptamolybdate) and 100 μL of an ascorbic acid solution (0.4 mol L^{-1}) were added to 3 ml of the diluted sample solution. Blue color was allowed to develop for 30 min and absorbance values were measured with a Hach & Lange, DR 2800 spectrophotometer at 880 nm in 1 cm disposable PS cells. Because of the reducing property of dithionite and the interfering organic ligands from the sodium citrate in the solution generated in step II (P_{Fe}), it is not possible to measure the phosphate concentrations using the ascorbic acid method (Ruttenberg, 1992). Instead P_{Fe} was obtained by subtraction (see below).

To calculate the phosphate concentrations from the measured absorbance values a standard calibration curve was established. Because interferences caused by the different reagents used in the SEDEX procedure may influence the measurement, matrix matched standard solutions were prepared from a phosphate stock solution ($1,000 \text{ mg L}^{-1} \text{ PO}_4^{3-}$). Linear regression analysis was performed by relating the concentration of phosphate in the standard solutions to the measured absorbance value. The resulting equation was used to calculate the concentrations in the sample solutions (fit better than $R^2 = 0.99$ in all cases). Sample solutions were diluted with 0.1 M HCl or H_2O UP to be bracketed by the concentrations of the respective standard solutions. Finally, the concentrations of the different phosphate fractions in the sample powders (c_{sample} in mg g^{-1}) were obtained from the concentration of the respective solutions (c_{sol} in mg L^{-1}), the volume of the solutions (V_{sol} in L) and the sample weights (m_{sample} in g) by following equation:

$$c_{\text{sample}} = \frac{c_{\text{sol}} \cdot V_{\text{sol}}}{m_{\text{sample}}} \quad (2)$$

To perform a background correction and to check for potential contamination during the SEDEX procedure two procedural blanks were included in each run of twelve samples. Average absorbance of the blank solutions was subtracted from the absorbance values of the samples prior to calculating concentrations. In order to estimate precision of the whole method an internal standard was processed and measured along every twelve samples (Table 1). Reproducibility for the concentration of P_{react} was $\pm 0.06 \text{ mg g}^{-1}$ ($n = 8$; RSD = 6%).



Major and Trace Element Analyses and Calculation of $\text{Ni}_{\text{excess}}$

Bulk major and trace element concentrations were measured via ICP-AES and ICP-MS on bulk rock powders after lithium borate fusion and four acid digestion at ALS Global Ltd. Analytical precision was better than 10% (RSD). For the

presentation of the Ni data, we used $\text{Ni}_{\text{excess}}$ which is the concentration of bulk Ni minus terrigenous Ni. This was done because Ni in bulk rock samples should be comprised of a terrigenous and an authigenic fraction. Enrichment factors ($\text{EF} = (\text{Ni}/\text{Al}_{\text{sample}})/(\text{Ni}/\text{Al}_{\text{PAAS}})$) were not calculated because our samples were mainly carbonates and cherts and because the

TABLE 2 | Average geochemical values for phase I (*C. transcaucasia* to lower *C. yini*) and III (upper *H. praeparvus* to *N. dieneri*) in the Chibi section and inferred P burial efficiency and primary productivity states. Samples with negative Ni_{excess} are interpreted to reflect no enrichment.

	TOC (%)	Ni_{excess} (ppm)	P_{react} (mg/g)	P_{Fe}/P_{tot}	C/P _{org}	P burial eff.	Productivity
Phase I	1.4	20.7	0.8	0.03	~2,900	-	High
Phase III	0.05	-2.4	0.1	0.12	~130	+	Low

PAAS reference for EF calculation is a shale. Ni_{excess} values were calculated as

$$Ni_{excess} = Ni_{sample} - \left(Al_{sample} \cdot \left(\frac{Ni}{Al} \right)_{PAAS} \right) \quad (3)$$

where $(Ni/Al)_{PAAS}$ is the Ni to Al ratio of average Post-Archean Australian shale ($(Ni/Al)_{PAAS} = 5.49 \times 10^{-4}$; Taylor and McLennan, 1985). In principle, the calculation of excess contents assumes that the Ni content of the terrigenous input was close to PAAS and that there was no variation in Ni/Al over the studied time interval. Values <0 are interpreted to reflect no authigenic Ni enrichment.

Calculation of Reactive Phosphorus (P_{react}), Fe-Oxyhydroxide Bound Phosphorus (P_{Fe}), and C/P Molar Ratios

Assuming that all P species, except for P_{det} , were bioavailable before sedimentation, the concentration of P_{react} was calculated by subtracting the concentration of P_{det} from the concentration of P_{tot} :

$$P_{react} = P_{tot} - P_{det} \quad (4)$$

P_{Fe} was determined by subtracting all P fractions determined via the ascorbic acid method (steps I, III, IV and V) from P_{tot} :

$$P_{Fe} = P_{tot} - (P_{ex} + P_{auth} + P_{det} + P_{org}) \quad (5)$$

C/P molar ratios were calculated as follows:

$$C/P_{react} = \frac{C/M(C)}{P_{react}/M(P)} \quad (6)$$

$$C/P_{org} = \frac{C/M(C)}{P_{org}/M(P)} \quad (7)$$

where M(C) and M(P) are the molar masses of carbon and phosphorus, respectively.

RESULTS

Stable Carbon Isotopes

Changhsingian $\delta^{13}C_{carb}$ values in the Chibi section vary between 1.2 and 2.5‰ (avg. = 1.85‰, $1\sigma = \pm 0.45\%$, $n = 6$; **Figure 5A; Supplementary Table S1**) until they start to increase at 5.83 m below the P-T boundary to values between 2.2 and 3.6‰ (avg. = 2.97‰, $1\sigma = \pm 0.55\%$, $n = 11$). Values start to decrease sharply by almost 3‰ at 1.2 m below the P-T boundary (upper *C. yini*

conodont Zone) to a minimum value of 0.1‰ at 0.63 m above the P-T boundary (*I. isarcica* Zone). This negative shift is followed by a gradual increase in $\delta^{13}C_{carb}$ in the Early Triassic with the stratigraphically highest sample showing a value of 1.1‰. For a discussion of the Chanakhchi carbon isotope record the reader is referred to Joachimski et al. (2020).

Total Organic Carbon and Ni_{excess}

In the lower part of the Chibi section, TOC values range from 0.15 to 2.17% (avg. = 1.39%, $1\sigma = \pm 0.64\%$, $n = 14$; **Figure 5A; Supplementary Table S1**). After this, they start to decrease 1.4 m below the P-T boundary (upper *C. yini* Zone) with average contents of 0.05% ($1\sigma = \pm 0.02\%$, $n = 32$) measured from 0.6 m below the P-T boundary to the Early Triassic. Samples from the Chanakhchi section show average TOC contents of 0.01% ($1\sigma = \pm 0.016\%$, $n = 42$) with only minor, statistically insignificant variation throughout the studied interval (**Figure 5B; Supplementary Table S2**). In general, such extremely low TOC contents should be treated with caution. Potentially, small flaws during sample preparation using the above-described method could result in artificially low values. Hence the TOC record from Chanakhchi is not interpreted in terms of relative changes because they are obviously below reproducibility of the data.

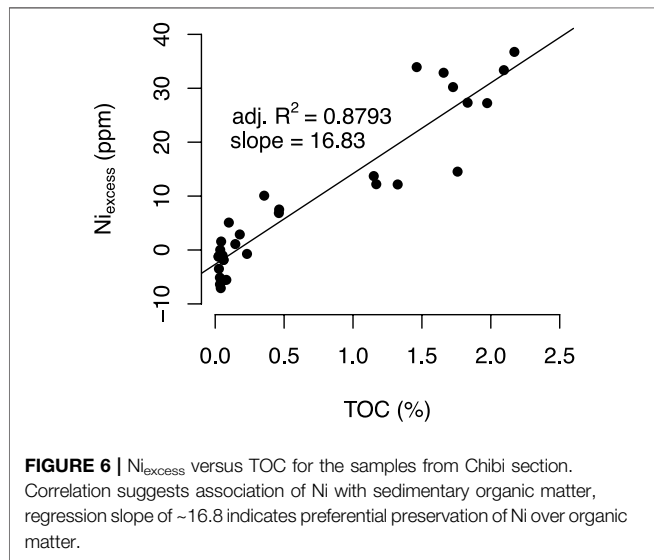
Ni_{excess} values in the Chibi section are between 1.1 and 36.7 ppm (avg. = 18.9 ppm, $1\sigma = \pm 12.4$ ppm, $n = 16$; **Figure 5A; Supplementary Table S1**) in the lower part of the studied section (Changhsingian) and decrease to <0 at 1.2 m below the P-T boundary (*C. yini* to *H. praeparvus* Zone). Upsection Ni_{excess} increases slightly and values stabilize close to 0. High and variable Ni_{excess} values between 6.1 and 18.7 ppm (avg. = 10.2 ppm, $1\sigma = \pm 4.6$ ppm, $n = 6$) are observed in the Chanakhchi section in the *C. transcaucasia* to *C. bachmanni* Zone (**Figure 5B; Supplementary Table S2**). Ni_{excess} starts to decrease 4.7 m below the P-T boundary and reaches values <0 in the uppermost *H. praeparvus* Zone. Upwards Ni_{excess} stays below 0 with two samples (Ch217 and Ch207) showing very negative values between the *I. isarcica* and *N. dieneri* zones.

Reactive Phosphorus (P_{react})

P_{react} in the latest Changhsingian of the Chibi section is highly variable with values between 0.04 and 1.46 mg g⁻¹ (**Figure 5A; Supplementary Table S1**). Two exceptionally high values of 3.13 and 9.14 mg g⁻¹ are observed at 9.4 and 1 m below the P-T boundary, respectively (samples Y14 and Z2). P_{react} contents decrease at 0.8 m below the P-T boundary (*H. praeparvus* Zone) and vary between 0.06 and 0.26 mg g⁻¹ (avg. = 0.14 mg g⁻¹, $1\sigma = \pm 0.06$ mg g⁻¹; $n = 14$) in the uppermost Changhsingian and Griesbachian. P_{react} in the Chanakhchi

TABLE 3 | Average geochemical values for phase I (*C. transcaucasia* to lower *C. yini*) and III (upper *H. praeparvus* to *N. dieneri*) in the Chanakhchi section and inferred P burial efficiency and primary productivity states.

	TOC (%)	Ni _{excess} (ppm)	P _{react} (mg/g)	P _{Fe} /P _{tot}	C/P _{org}	P burial eff.	Productivity
Phase I	0.01	10.2	0.4	0	~24	+	High
Phase III	0.01	-0.2	0.1	0.42	~40	+	Low



section also exhibits a downward trend towards the P-T boundary, albeit the decrease in P_{react} appears more gradual than in the Chibi section (**Figure 5B**; **Supplementary Table S2**). The highest value of 0.92 mg g⁻¹ is observed 10.6 m below the P-T boundary in the *C. transcaucasia* Zone (sample Ch37). Above this level, values decline gradually and vary around an average of 0.11 mg g⁻¹ (1σ = ±0.06 mg g⁻¹, n = 36) in the *H. praeparvus* Zone and the Early Triassic. Hence, both sections show a significant decrease in P_{react} from the Lopingian into the Early Triassic.

Fe-Oxyhydroxide Bound Phosphorus (P_{Fe})

In both sections, the proportion of P_{Fe} relative to P_{tot}, expressed as the ratio P_{Fe}/P_{tot}, is elevated in specific time intervals (**Figure 5**). We used a P_{Fe}/P_{tot} ratio >0.2 to characterize intervals where P_{Fe} represents an important P fraction. This estimate is based on modern, global P burial flux calculations showing that P_{Fe} contributes ~20% to the total reactive P flux to the sediment (Ruttenberg, 1993). In the Chibi section, P_{Fe}/P_{tot} ratios >0.2 are observed in the *C. yini* to *H. praeparvus* Zones (1.4–1 m below the P-T boundary) and in the *I. isarcica* Zone (0.9–2.7 m above the P-T boundary). At Chanakhchi, P_{Fe}/P_{tot} > 0.2 are registered in the *C. nodosa* and *C. zhangi* Zones (4.1 and 2.9 m below the P-T boundary) and in an interval starting 1.6 m below the P-T boundary, from the *H. praeparvus* to the *N. dieneri* Zone (avg. = 0.42, 1σ = ±0.19, n = 22). In the latter interval, three samples show P_{Fe}/P_{tot} < 0.2. In all other samples, P_{Fe} is a minor fraction of P_{tot} with P_{Fe}/P_{tot} < 0.2.

C/P Molar Ratios

At Chibi, C/P_{org} ratios range from 254 to 5,780 (avg. = 2,576, 1σ = ±1861, n = 16) in the Changhsingian and start to decrease at 1.2 m below the P-T boundary (*C. yini* to *H. praeparvus* Zone; **Figure 5A**; **Supplementary Table S1**). Values in the uppermost Changhsingian and Griesbachian fluctuate between 20 and 328 (avg. = 119, 1σ = ±96, n = 15). C/P_{react} ratios are lower than the C/P_{org} ratios. C/P_{react} values are between 3 and 318 (avg. = 108, 1σ = ±112, n = 16) and decrease in parallel with C/P_{org} to low values between 1 and 17 (avg. = 9, 1σ = ±5, n = 15). At Chanakhchi, C/P ratios show no significant change but C/P_{org} values of 12–122 (avg. = 39, 1σ = ±31, n = 14) are higher than C/P_{react} values between 0 and 17 (avg. = 4, 1σ = ±4, n = 19) throughout the studied interval (**Figure 5B**; **Supplementary Table S2**).

DISCUSSION

For the discussion of the dataset, three temporal intervals are defined based on the stratigraphic variation in Ni_{excess}. Phase I (*C. transcaucasia* to lower *C. yini* Zone) is characterized by high TOC in the Chibi section and generally high Ni_{excess} values in both sections. Phase II (upper *C. yini* to lower *H. praeparvus* Zone) represents a transitional interval with decreasing, intermediate Ni_{excess} values, while during phase III (upper *H. praeparvus* to *N. dieneri* Zone), low TOC and low Ni_{excess} values are observed in both sections (see **Tables 2, 3**).

Nickel as Paleoproductivity Proxy

TOC as a paleoproductivity proxy has major shortcomings since the TOC contents might be biased due to remineralization of organic matter in the water column, anaerobic decomposition of organic matter during diagenesis, and the dilution effect (e.g., Schoepfer et al., 2015). Thus, only a fraction of organic matter exported from surface waters sinks to the seafloor and is preserved in sediments. Ni_{excess} is used as another productivity proxy as it shows a nutrient-like distribution in the water column and, in case of anoxic conditions, is less prone to co-precipitation with sulfides compared to Cu, Cd, or Zn (Piper and Calvert, 2009). Furthermore, stable Ni isotope data suggests that the distribution of Ni in the water column is not affected by redox cycling (Yang et al., 2021). Recent studies showed that Ni and TOC are positively correlated in modern, superficial sediments regardless of redox conditions making Ni a robust and reliable productivity proxy (Böning et al., 2015; Steiner et al., 2017). For example, Steiner et al. (2017) were able to link anthropogenic nutrient fluxes and associated

productivity changes to sedimentary Ni concentrations in oxic sediments of the Gulf of Aqaba.

Ni_{excess} shows decreasing concentrations from phase I to phase III in both study sections (Figure 5). Ni_{excess} is positively correlated with TOC in the Chibi section ($R^2 = 0.88$, $p < 0.001$; Figure 6) suggesting that Ni was mainly shuttled to the sediment by sinking organic matter. The slope of the linear regression is 16.8 and thus higher than for modern core top sediments (~6–9; Böning et al., 2015) suggesting preferential preservation of Ni over TOC during sinking, burial, and diagenesis. Furthermore, this correlation indicates that the preservation factor of organic matter remained invariant over the studied interval in case of the Chibi section. In contrast, samples from the Chanakhchi section point towards lower preservation of organic matter in phase I, since we observe no change in TOC (~0.01%) but a decrease in Ni_{excess} from phase I to III. The decrease in Ni_{excess} in both sections is interpreted as the result of declining primary productivity in the Tethys Ocean starting in the *C. yini* Zone. For the following discussion Ni_{excess} values from Chanakhchi serve as a surrogate for the primary TOC content of the sediment, i.e., Chanakhchi samples with high Ni_{excess} are interpreted to reflect a high organic matter sinking flux and vice versa.

In this study we use Ni contents as a proxy for the sinking flux of organic matter because Ni is an essential nutrient for photosynthesizing organisms. However, an alternative source of Ni could be through the deposition of Ni-rich aerosols released to the atmosphere during Siberian Traps volcanism (Le Vaillant et al., 2017). Indeed, peaks in Ni contents coinciding with the negative shift in $\delta^{13}C$ were reported for several P-T sections (Rothman et al., 2014; Rampino et al., 2017; Li et al., 2021). Furthermore, Li et al. (2021) found that Ni-rich beds of the Buchanan Lake section exhibit extremely light Ni stable isotopic compositions corroborating a volcanogenic signature ($\delta^{60}Ni$ down to -1.09%). In contrast the Ni-records from Chibi and Chanakhchi are not showing such a relationship, i.e., Ni contents are already low when the negative excursion in $\delta^{13}C$ starts (Figure 5). Hence, we argue that the Lopingian high Ni_{excess} values of this study are unrelated to P-T volcanism and reflect high organic matter sinking fluxes.

P Scavenging From the Water Column

In the case of anoxic conditions and Fe-oxide reduction, P bound to Fe-oxides will be released to the water column or porewaters and potentially reprecipitated as authigenic P-minerals (sink switching; Paytan and McLaughlin, 2007). The increase in $P_{\text{Fe}}/P_{\text{tot}}$ from phase I to II (Figure 5) coincides with the observed decrease in Ni_{excess} in both sections. At Chibi, TOC decreases with rising $P_{\text{Fe}}/P_{\text{tot}}$. Hence the data show an inverse relationship and two cases can be differentiated. Samples from Chanakhchi with low $P_{\text{Fe}}/P_{\text{tot}}$ show high Ni_{excess} while high $P_{\text{Fe}}/P_{\text{tot}}$ appears together with low Ni_{excess} and TOC. At Chibi the same relationship is observed for $P_{\text{Fe}}/P_{\text{tot}}$ and Ni_{excess} and additionally samples with low $P_{\text{Fe}}/P_{\text{tot}}$ show high TOC contents.

This pattern has been observed as well in modern sediments from the California continental margin where sediments are deposited in low O_2 bottom waters and P is either released or

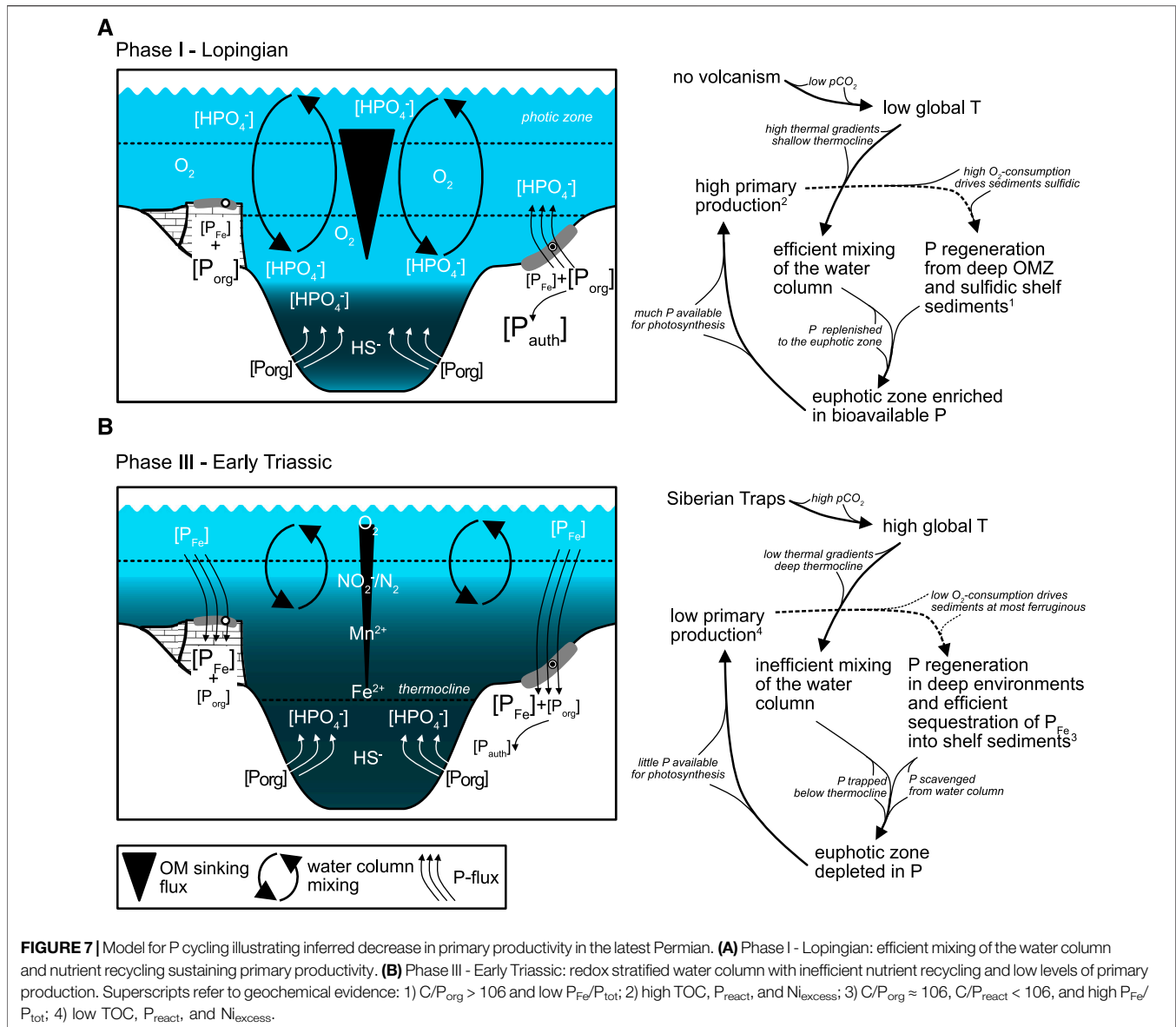
sequestered with Fe-oxides depending on the amount of organic matter remineralization (McManus et al., 1997). P is sequestered into the sediment when little organic matter is available for decomposition and vice versa. McManus et al. (1997) attribute this to the presence of a ferric layer within the upper part of the sediments providing sites for P adsorption. The ferric layer only develops if O_2 consumption through organic matter remineralization is not too high and the depth of O_2 penetration is intermediate.

Relatively high TOC and/or Ni_{excess} values in combination with minor or absent P_{Fe} contents in phase I samples indicate the release of P_{Fe} during the reductive dissolution of Fe-oxides in a sediment where free oxygen was effectively consumed by organic matter degradation which shifted sediment redox conditions below the zone of Fe^{3+} reduction (further supported by high C/P_{react} at Chibi). In contrast, O_2 consumption through organic matter remineralization was likely minor in phases II and III as signaled by low sedimentary TOC and/or Ni_{excess} . Redox conditions not below the zone of nitrate or Mn^{4+} reduction would have favored the formation of ferric layers which served as an efficient P sink (further supported by low C/P_{react}). This can explain the preservation of high P_{Fe} proportions in the phase III samples.

Benthic P Regeneration and/or Reduced P-Shuttle

Both sections show a significant decrease in average P_{react} concentrations from phase I to phase III (Figure 5; Tables 2, 3). This decrease can be explained either by benthic P regeneration causing a decrease in the P burial efficiency and therefore low P contents in sediments (Ingall and Jahnke, 1994) or a lower primary productivity since, besides Fe-oxyhydroxide, organic matter is the main shuttle of reactive P to the sediment (Paytan and McLaughlin, 2007).

Studies on modern, subrecent and deep time sediments have shown that P is preferentially released from the sediment to the water column under anoxic conditions (e.g., Van Cappellen and Ingall, 1994; Filippelli et al., 2003; Mort et al., 2007; Fantasia et al., 2018; Schobben et al., 2020). While the release of P_{Fe} is in the form of reductive dissolution of Fe-oxides, the enhanced release of P_{org} seems to be microbially mediated; i.e., the bacterial sequestration of P into stable polyphosphates is less efficient under anoxic conditions because only some P-accumulating bacteria are able to utilize nitrate as an electron acceptor for this process (Kern-Jespersen and Henze, 1993). In the case where dissolved P is transferred to the euphotic zone e.g., by diffusion, mixing of the water column or upwelling, it can be utilized by phytoplankton. In such case, P may increase primary productivity, expand the oxygen-minimum zone, and reinforce the sinking flux of organic carbon in a positive feedback loop (Van Cappellen and Ingall, 1994; Mort et al., 2007). The efficiency of water column mixing depends on the wind intensity, the depth of the thermocline, and the degree of thermal stratification (Kämpf and Chapman, 2016). Substantial warming from the latest Permian into the Early Triassic (e.g., Joachimski et al., 2012; Joachimski et al., 2020) likely resulted in decreased wind stress, a deeper thermocline, and



enhanced stratification of the water column (e.g., Hotinski et al., 2001; Kidder and Worsley, 2004). Hence, we argue that the vertical P-shuttle was likely less efficient during the latest Permian to Early Triassic, leading to P-trapping in a large deep water P-reservoir (Penn et al., 2018).

P_{react} concentrations are comparably variable ($0.04\text{--}1.46\text{ mg g}^{-1}$) during phase I in the Chibi section (Figure 5A). Filippelli et al. (2003) explained varying P_{react} concentrations in late Miocene sapropels as a consequence of precessional wind systems resulting in alternating water column stratification (low productivity, low particulate organic matter (POM)-shuttle, low net P-burial, high P-release, low P_{react} , P accumulation in deep water) and intense upwelling (high productivity, high POM-shuttle, high net P-burial, low P-release, P recycled to euphotic zone). This scenario is likely

an analogue for phase I at Chibi. Accordingly, low P_{react} values would correspond to intervals with low productivity and P accumulation whereas higher P_{react} values would correspond to intervals with high productivity where deep-water P was effectively replenished to the euphotic zone through water column mixing. In phase III, P_{react} is low (avg. = 0.14 mg g^{-1}) and less variable, again, pointing to enhanced water column stratification in the tropical Tethyan realm.

The molar ratio of organic carbon versus P_{org} and P_{react} (C/P_{org} and C/P_{react}) is used as an additional proxy to reconstruct benthic P-regeneration, the transfer of P into authigenic phases and hence the burial efficiency of P. While sinking organic matter has a stoichiometrical C/P ratio of 106 (Redfield et al., 1963), after sedimentation under anoxic conditions, P might be preferentially released increasing the C/P ratio of refractory organic matter to

>106 (Ingall et al., 1993). Released P can either be transferred to the upper water column where it can be re-used by primary production or precipitated as authigenic phosphate in the sediment (Paytan and McLaughlin, 2007). The latter mechanism is able to decrease C/P_{react} ratios to <106 since authigenic phosphate contributes to the P_{react} pool.

C/P_{org} ratios from the Chibi section are consistently >106 in phase I, indicating P loss during the deposition and burial of organic matter (Figure 5A). Intervals with $C/P_{\text{org}} > 106$ and $C/P_{\text{react}} < 106$ are characterized by sink switching processes, i.e., the transfer of P_{org} and P_{Fe} to authigenic carbonate fluorapatite. C/P_{org} and $C/P_{\text{react}} > 106$ can be attributed to intervals with strong P loss to the water column continuously depleting refractory organic matter with respect to P. P_{react} values below stoichiometrically possible concentrations of sinking organic matter are generated by this process in samples showing relatively high C/P_{react} ratios. Hence efficient P-recycling likely sustained high primary productivity levels in phase I. C/P_{org} ratios ≤ 106 in phase III suggest that efficient burial of P_{org} with benthic P-regeneration was likely inhibited. Low P_{react} concentrations together with $C/P_{\text{react}} < 106$ in phase III document a reduced organic matter shuttle. The high proportion of P_{Fe} in phase III can explain $C/P_{\text{react}} < 106$ because the P_{Fe} sink is decoupled from carbon cycling (see *P Scavenging From the Water Column*; McManus et al., 1997; Paytan and McLaughlin, 2007).

In Chanakhchi C/P_{org} is <106 and C/P_{react} is <106 throughout the sampled interval (Figure 5B). Like in Chibi, the latter is explained by the relatively high proportion of P_{Fe} . $C/P_{\text{org}} < 106$ indicates that there was neither an active sink switch nor P loss to the water column, thus burial efficiency was high at any given time. As previously noted, sample preparation as well as organic matter remineralization might have affected C/P ratios by lowering TOC contents. However, if TOC contents were 10 times higher the calculation of C/P ratios would still give values indicative of efficient P burial.

Changes in Primary Productivity Across the P-T Boundary

A conceptual model was developed to explain changes in marine P cycling in the Tethys across the P-T boundary (Figure 7). Primary productivity was comparably high during the Lopingian (phase I), started to decline in the upper *C. yini* conodont Zone (phase II) and was at lower levels during the final Changhsingian and subsequent Early Triassic (phase III; Jiang et al., 2007; Chen et al., 2015). This interpretation is based on the observation that TOC and Ni_{excess} (at Chanakhchi only Ni_{excess}) contents decrease significantly across the transitional phase II and the assumption that the two proxies behave proportional to the organic matter sinking flux and thus primary productivity.

High productivity in the tropical Tethys Ocean during the Lopingian is indicated by high P_{react} concentrations in both sections. P burial efficiency was low at Chibi but high at Chanakhchi as suggested from C/P ratios. This suggests that at

Chibi a large part of the sedimentary P delivered by sinking organic matter and Fe-oxides was lost to the water column or transferred to authigenic P phases under O_2 deficient conditions driven by organic matter remineralization. Because mixing of surface and bottom waters was likely more efficient during the cooler climatic conditions of the Permian, recycled P was replenished to the euphotic zone, fueling photosynthesis and sustaining productivity on equatorial shelves. This eventually led to the observed enrichment of authigenic P. However, low C/P ratios at Chanakhchi indicate that sedimentary P was not recycled but buried efficiently in shallow platform environments.

Low P_{react} concentrations together with low C/P_{org} ratios indicate efficient P burial, corroborating the latest Permian to Early Triassic low productivity scenario for the tropical Tethys. Although there was no P loss from the sediment, concentrations of P_{react} are low at both sites. Under the exceptional warmth of the Early Triassic, vertical mixing in the water column was probably inhibited when a deep thermocline was developed (Kidder and Worsley, 2004; Grasby et al., 2016; Grasby et al., 2020). Hence, although it is possible that P-regeneration occurred in other euxinic deeper water settings, P still would have been trapped in bottom waters.

P_{Fe} became a relatively important P sink in the latest Permian to Early Triassic (phase III). P trapping in bottom waters combined with Fe-oxide associated scavenging of bioavailable P from the water column and efficient burial in shelf and platform sediments possibly caused P depletion in the euphotic zone of the Tethys Ocean. A prerequisite for such scenario is that bottom waters and sediment redox conditions did not exceed the ferruginous zone. This is plausible since there was probably no significant O_2 consumption via organic matter remineralization to shift redox conditions into the sulfidic zone (TOC is low; anoxia is controlled by stratification). Furthermore, this interpretation is consistent with modeling and geochemical studies pointing towards less severe O_2 depletion in the upper water column of the tropical oceans (Clarkson et al., 2016; Penn et al., 2018). These conditions might have been similar to pre-Cryogenian oceans when pervasive ferruginous conditions resulted in enhanced scavenging of P from surface waters and low P burial on continental margins in the form of authigenic phosphates (Reinhard et al., 2017). Accordingly, we argue that, during the latest Permian to Early Triassic (phase III), the water column in the low-latitude Tethys was characterized by warm oligotrophic surface waters with nutrient trapping occurring in deeper anoxic waters (Grasby et al., 2016). P shuttling to the sediment diminished with the decrease in marine primary productivity (Algeo et al., 2013).

According to this model, an eutrophication scenario in the Tethys Ocean is untenable. Schobben et al. (2020) argued for a boost in primary productivity followed by eutrophication as a consequence of enhanced nutrient input and P recycling. The dataset, spanning the extinction interval to the Early Triassic, was acquired in a mid-latitude setting at the northern margin of Pangea (Deltadalen and Festningen, Spitsbergen). On the

other hand, stable nitrogen isotopes from the same region (Festningen; Grasby et al., 2020) and from virtually all P-T boundary sections exhibit a significant decrease in $\delta^{15}\text{N}$ across the extinction interval, indicating a shift to dominance of diazotrophic metabolism and a substantial decrease in the oceanic nutrient-N inventory, leading to oligotrophic oceans (e.g., Schoepfer, 2013; Sun et al., 2019). This discrepancy in interpretations is due to either the application of different proxies, or simply to the fact that there are contrasts between distal and proximal sites in respect to nutrient influx. However, a collapse of primary productivity is documented not only in northern low- and mid-latitudes, but also in the southern mid-latitude oceans (Sun et al., 2021). In general, regional differences in the effect of global warming on marine primary productivity are to be expected, given that climate models predictions for the modern ocean are spatially heterogeneous (e.g., Mora et al., 2013).

Decline of Primary Production and its Effects on Marine Food Webs

In both sections, the transitional phase II starts slightly earlier than the onset of the negative carbon isotope excursion and ends before the $\delta^{13}\text{C}_{\text{carb}}$ curves reach their minima in the *H. parvus* Zone (Figure 5). Thus, in both sections, the decline in primary productivity coincides with the major part of the negative shift in $\delta^{13}\text{C}_{\text{carb}}$. Using the radiometric ages from the Meishan GSSP section, conodont biozonation and assuming constant sedimentation rate, it can be estimated that primary productivity started to decrease approximately 30 ka before the main extinction interval (Jiang et al., 2007; Burgess et al., 2014; Chen et al., 2015). Since marine primary producers constitute the base of marine food webs, their decline likely imposed negative effects on higher trophic levels.

Body size reduction and biodiversity losses among marine heterotrophic organisms have been reported for the pre-extinction interval. For example, brachiopods from South China show miniaturization starting in the *C. yini* Zone and community turnover occurred prior to the onset of the main phase of marine extinction (Zhang et al., 2016). Besides higher water temperatures or lower oxygen levels, declining primary productivity serves as an explanation for miniaturization since reduced body size can be an adaptation to a decrease in food supply (e.g., Yasuda et al., 2016). Sponge spicules exhibit a significant decline in abundance, size and morphological diversity in an interval corresponding to the upper *C. yini* conodont Zone (Liu et al., 2013). Radiolarians suffered significant diversity loss before the extinction with ~53% of species and ~22% of genera going extinct in the *C. yini* Zone (Meishan Bed 24d; Feng et al., 2007). A first extinction pulse among *Albaillella* observed in pelagic sections from Japan can be correlated with the aforementioned event (Wenchen et al., 2004). In the western Tethys, ammonoids from Iran exhibit an extinction pulse as well as declining morphological complexity and body size (pedomorphosis) in the *Paratirolites kittli* ammonoid Zone which is equivalent to the

C. yini conodont Zone (Kiessling et al., 2018). However, the authors erroneously claimed that this deterioration started 700 ka before the extinction not taking into account radiometric ages from the Meishan section indicating that the onset of the *C. yini* Zone is significantly younger (Burgess et al., 2014).

Hence, the decrease in primary productivity in the tropical Tethys can be temporally correlated with the prelude of the extinction. However, at least in some regions, oxygen availability in the water column decreased at the same time (e.g., Clarkson et al., 2016). Hence, the expansion of oxygen minimum zones is an equally valid explanation. In general, anoxia directly stresses marine organisms by narrowing suitable habitats for sensitive species. Considering an inverse relationship between marine primary productivity and anoxia under warming climatic conditions it turns out that both are inextricably connected (Keeling et al., 2010). This is because mixing of oxygenated and nutrient-poor surface waters with deoxygenated and nutrient-rich deeper waters is diminished when water column stratification becomes stronger.

SUMMARY

Downward trends in sedimentary productivity proxies (TOC, $\text{Ni}_{\text{excess}}$, and P_{react}) from two Tethyan successions suggest a reduction of the organic matter sinking flux due to a decrease of marine primary productivity from the Lopingian to the Early Triassic. This commenced in the upper *C. yini* conodont Zone 30 ka before the main marine extinction level. C/P ratios indicate a switch from efficient P-recycling during the Lopingian normal productivity interval to efficient P-burial during the low productivity interval with Fe-oxides becoming a major P sink in the Early Triassic.

The decrease in primary productivity in the equatorial Tethyan realm can be explained by the concomitant effects of global warming across the P-T boundary, in particular enhanced stratification of the water column and a deepened thermocline leading to a state of inefficient P recycling. Hence, the latest Permian and Early Triassic Tethys was characterized by nutrient-poor surface waters while deep waters were probably enriched in P released from pelagic euxinic sediments. Potentially, the described developments reflect the onset of the Early Triassic Phosphorite gap, i.e., the lacking deposition of P-rich marine sediments for almost 5 Ma due to nutrient stress (Trappe, 1994). While this was demonstrated for the western, northern and eastern margins of Pangea (Schoepfer, 2013; Grasby et al., 2016; Grasby et al., 2020; Sun et al., 2021) our results suggest a similar oligotrophication scenario for the tropical Tethys Ocean.

The resulting food shortage may explain coincident extinction pulses, reductions in body size and pedomorphosis among heterotrophic organisms particularly in the tropical Tethys before and during the end-Permian mass extinction interval as well as during the protracted recovery phase.

DATA AVAILABILITY STATEMENT

The original contributions presented in the study are included in the article/**Supplementary Material**, further inquiries can be directed to the corresponding authors.

AUTHOR CONTRIBUTIONS

JM designed the study, generated, and analyzed the datasets and wrote the manuscript. YS designed the study and revised the manuscript. FY and AF generated and analyzed data. MJ designed the study, revised the manuscript, and is the project administration.

FUNDING

The National Natural Science Foundation of China (grant no. 41821001) supported this study. This is a contribution to German Research Foundation (DFG) Research Unit TERSANE (FOR 2332: Temperature-related stressors as a unifying principle in ancient extinctions; Project Jo 219/16-1).

REFERENCES

- Algeo, T. J., and Twitchett, R. J. (2010). Anomalous Early Triassic Sediment Fluxes Due to Elevated Weathering Rates and Their Biological Consequences. *Geology* 38, 1023–1026. doi:10.1130/G31203.1
- Algeo, T. J., Henderson, C. M., Tong, J., Feng, Q., Yin, H., and Tyson, R. V. (2013). Plankton and Productivity during the Permian-Triassic Boundary Crisis: An Analysis of Organic Carbon Fluxes. *Glob. Planet. Change* 105, 52–67. doi:10.1016/j.gloplacha.2012.02.008
- Aspila, K. I., Agemian, H., and Chau, A. S. Y. (1976). A Semi-automated Method for the Determination of Inorganic, Organic and Total Phosphate in Sediments. *Analyst* 101, 187–197. doi:10.1039/an9760100187
- Bambach, R. K., Knoll, A. H., and Wang, S. C. (2004). Origination, Extinction, and Mass Depletions of marine Diversity. *Paleobiology* 30, 522–542. doi:10.1666/0094-8373(2004)030<0522:oeamdo>2.0.co;2
- Baud, A., Richoz, S., and Pruss, S. (2007). The Lower Triassic Anachronistic Carbonate Facies in Space and Time. *Glob. Planet. Change* 55, 81–89. doi:10.1016/j.gloplacha.2006.06.008
- Behrenfeld, M. J., O'Malley, R. T., Siegel, D. A., McClain, C. R., Sarmiento, J. L., Feldman, G. C., et al. (2006). Climate-Driven Trends in Contemporary Ocean Productivity. *Nature* 444, 752–755. doi:10.1038/nature05317
- Böning, P., Shaw, T., Pahnke, K., and Brumsack, H.-J. (2015). Nickel as Indicator of Fresh Organic Matter in Upwelling Sediments. *Geochim. Cosmochim. Acta* 162, 99–108. doi:10.1016/j.gca.2015.04.027
- Bond, D. P. G., and Grasby, S. E. (2017). On the Causes of Mass Extinctions. *Palaeogeogr. Palaeoclimatol. Palaeoecol.* 478, 3–29. doi:10.1016/j.palaeo.2016.11.005
- Bopp, L., Resplandy, L., Orr, J. C., Doney, S. C., Dunne, J. P., Gehlen, M., et al. (2013). Multiple Stressors of Ocean Ecosystems in the 21st century: Projections with CMIP5 Models. *Biogeosciences* 444, 6225–6245. doi:10.5194/bg-10-6225-2013
- Boyd, P. W., Sundby, S., and Pörtner, H.-O. (2014). “Cross-Chapter Box on Net Primary Production in the Ocean,” in *Climate Change 2014: Impacts, Adaptation, and Vulnerability. Part A: Global and Sectoral Aspects. Contribution of Working Group II to the Fifth Assessment Report of the Intergovernmental Panel of Climate Change* (Cambridge University Press), 133–136.
- Burgess, S. D., Bowring, S., and Shen, S.-z. (2014). High-precision Timeline for Earth's Most Severe Extinction. *Proc. Natl. Acad. Sci. USA* 111, 3316–3321. doi:10.1073/pnas.1317692111

ACKNOWLEDGMENTS

We acknowledge logistic support and advice during fieldwork in South China by Prof. Y.B. Wang (CUG Wuhan) who sadly passed away in early 2021 before this study was accomplished. We thank Thierry Adatte (University of Lausanne/Switzerland) for kindly granting access to the phosphorus lab at UNIL and Daniele Lutz (FAU Erlangen-Nürnberg) for measuring carbon isotopes and organic carbon contents. Tan Wang and Yujun Bao (CUG Wuhan) are acknowledged for great help with collecting samples from the Chibi section. Johannes Barth, Christian Hanke, and Robert van Geldern (FAU Erlangen-Nürnberg) are thanked for analytical support. Furthermore, we thank two reviewers for their constructive comments.

SUPPLEMENTARY MATERIAL

The Supplementary Material for this article can be found online at: <https://www.frontiersin.org/articles/10.3389/feart.2022.832308/full#supplementary-material>

- Burgess, S. D., Muirhead, J. D., and Bowring, S. A. (2017). Initial Pulse of Siberian Traps Sills as the Trigger of the End-Permian Mass Extinction. *Nat. Commun.* 8, 164. doi:10.1038/s41467-017-00083-9
- Burnett, W. C., Beers, M. J., and Roe, K. K. (1982). Growth Rates of Phosphate Nodules from the Continental Margin off Peru. *Science* 215, 1616–1618. doi:10.1126/science.215.4540.1616
- Chen, Z.-Q., Yang, H., Luo, M., Benton, M. J., Kaiho, K., Zhao, L., et al. (2015). Complete Biotic and Sedimentary Records of the Permian-Triassic Transition from Meishan Section, South China: Ecologically Assessing Mass Extinction and its Aftermath. *Earth-Science Rev.* 149, 67–107. doi:10.1016/j.earscirev.2014.10.005
- Chen, J., Shen, S.-z., Zhang, Y.-c., Angiolini, L., Gorgij, M. N., Crippa, G., et al. (2020). Abrupt Warming in the Latest Permian Detected Using High-Resolution *In Situ* Oxygen Isotopes of Conodont Apatite from Abadeh, central Iran. *Palaeogeogr. Palaeoclimatol. Palaeoecol.* 560, 109973. doi:10.1016/j.palaeo.2020.109973
- Clarkson, M. O., Wood, R. A., Poulton, S. W., Richoz, S., Newton, R. J., Kasemann, S. A., et al. (2016). Dynamic Anoxic Ferruginous Conditions during the End-Permian Mass Extinction and Recovery. *Nat. Commun.* 7, 12236. doi:10.1038/ncomms12236
- Fantasia, A., Föllmi, K. B., Adatte, T., Spangenberg, J. E., and Montero-Serrano, J.-C. (2018). The Early Toarcian Oceanic Anoxic Event: Paleoenvironmental and Paleoclimatic Change across the Alpine Tethys (Switzerland). *Glob. Planet. Change* 162, 53–68. doi:10.1016/j.gloplacha.2018.01.008
- Feng, Q., He, W., Gu, S., Meng, Y., Jin, Y., and Zhang, F. (2007). Radiolarian Evolution during the Latest Permian in South China. *Glob. Planet. Change* 55, 177–192. doi:10.1016/j.gloplacha.2006.06.012
- Filippelli, G. M., Sierro, F. J., Flores, J. A., Vázquez, A., Utrilla, R., Pérez-Folgado, M., et al. (2003). A Sediment-Nutrient-Oxygen Feedback Responsible for Productivity Variations in Late Miocene Sapropel Sequences of the Western Mediterranean. *Palaeogeogr. Palaeoclimatol. Palaeoecol.* 190, 335–348. doi:10.1016/S0031-0182(02)00613-2
- Foster, W. J., Heindel, K., Richoz, S., Gliwa, J., Lehrmann, D. J., Baud, A., et al. (2020). Suppressed Competitive Exclusion Enabled the Proliferation of Permian/Triassic Boundary Microbialites. *Depositional Rec.* 6, 62–74. doi:10.1002/dep2.97
- Friesenbichler, E., Richoz, S., Baud, A., Krystyn, L., Sahakyan, L., Vardanyan, S., et al. (2018). Sponge-microbial Build-Ups from the Lowermost Triassic Chanakhchi Section in Southern Armenia: Microfacies and Stable Carbon Isotopes. *Palaeogeogr. Palaeoclimatol. Palaeoecol.* 490, 653–672. doi:10.1016/j.palaeo.2017.11.056

- Grasby, S. E., Beauchamp, B., Embry, A., and Sanei, H. (2013). Recurrent Early Triassic Ocean Anoxia. *Geology* 41, 175–178. doi:10.1130/g33599.1
- Grasby, S. E., Beauchamp, B., and Knies, J. (2016). Early Triassic Productivity Crises Delayed Recovery from World's Worst Mass Extinction. *Geology* 44, 779–782. doi:10.1130/G38141.1
- Grasby, S. E., Knies, J., Beauchamp, B., Bond, D. P. G., Wignall, P., and Sun, Y. (2020). Global Warming Leads to Early Triassic Nutrient Stress across Northern Pangea. *Geol. Soc. Am. Bull.* 132, 943–954. doi:10.1130/b32036.1
- Hotinski, R. M., Bice, K. L., Kump, L. R., Najjar, R. G., and Arthur, M. A. (2001). Ocean Stagnation and End-Permian Anoxia. *Geology* 29, 7. doi:10.1130/0091-7613(2001)029<0007:osaepa>2.0.co;2
- Ingall, E., and Jahnke, R. (1994). Evidence for Enhanced Phosphorus Regeneration from marine Sediments Overlain by Oxygen Depleted Waters. *Geochim. Cosmochim. Acta* 58, 2571–2575. doi:10.1016/0016-7037(94)90033-7
- Ingall, E. D., Bustin, R. M., and Van Cappellen, P. (1993). Influence of Water Column Anoxia on the Burial and Preservation of Carbon and Phosphorus in marine Shales. *Geochim. Cosmochim. Acta* 57, 303–316. doi:10.1016/0016-7037(93)90433-W
- Isozaki, Y. (1997). Permo-Triassic Boundary Superanoxia and Stratified Superocean: Records from Lost Deep Sea. *Science* 276, 235–238. doi:10.1126/science.276.5310.235
- Jiang, H., Lai, X., Luo, G., Aldridge, R., Zhang, K., and Wignall, P. (2007). Restudy of Conodont Zonation and Evolution across the P/T Boundary at Meishan Section, Changxing, Zhejiang, China. *Glob. Planet. Change* 55, 39–55. doi:10.1016/j.gloplacha.2006.06.007
- Joachimski, M. M., Lai, X., Shen, S., Jiang, H., Luo, G., Chen, B., et al. (2012). Climate Warming in the Latest Permian and the Permian-Triassic Mass Extinction. *Geology* 40, 195–198. doi:10.1130/G32707.1
- Joachimski, M. M., Alekseev, A. S., Grigoryan, A., and Gatovsky, Y. A. (2020). Siberian Trap Volcanism, Global Warming and the Permian-Triassic Mass Extinction: New Insights from Armenian Permian-Triassic Sections. *Geol. Soc. Am. Bull.* 132, 427–443. doi:10.1130/B35108.1
- Kämpf, J., and Chapman, P. (2016). *Upwelling Systems of the World*. Cham: Springer International Publishing. doi:10.1007/978-3-319-42524-5
- Keeling, R. F., Körtzinger, A., and Gruber, N. (2010). Ocean Deoxygenation in a Warming World. *Annu. Rev. Mar. Sci.* 2, 199–229. doi:10.1146/annurev.marine.010908.163855
- Kerrn-Jespersen, J. P., and Henze, M. (1993). Biological Phosphorus Uptake under Anoxic and Aerobic Conditions. *Water Res.* 27, 617–624. doi:10.1016/0043-1354(93)90171-D
- Kidder, D. L., and Worsley, T. R. (2004). Causes and Consequences of Extreme Permo-Triassic Warming to Globally Equable Climate and Relation to the Permo-Triassic Extinction and Recovery. *Palaeogeogr. Palaeoclimatol. Palaeoecol.* 203, 207–237. doi:10.1016/S0031-0182(03)00667-9
- Kiessling, W., Schobben, M., Ghaderi, A., Hairapetian, V., Leda, L., and Korn, D. (2018). Pre-mass Extinction Decline of Latest Permian Ammonoids. *Geology* 46, 283–286. doi:10.1130/G39866.1
- Kocsis, Á. T., and Scotese, C. R. (2021). Mapping Paleocoastlines and continental Flooding during the Phanerozoic. *Earth-Science Rev.* 213, 103463. doi:10.1016/j.earscirev.2020.103463
- Korte, C., and Kozur, H. W. (2010). Carbon-isotope Stratigraphy across the Permian-Triassic Boundary: A Review. *J. Asian Earth Sci.* 39, 215–235. doi:10.1016/j.jseas.2010.01.005
- Korte, C., Pande, P., Kalia, P., Kozur, H. W., Joachimski, M. M., and Oberhänsli, H. (2010). Massive Volcanism at the Permian-Triassic Boundary and its Impact on the Isotopic Composition of the Ocean and Atmosphere. *J. Asian Earth Sci.* 37, 293–311. doi:10.1016/j.jseas.2009.08.012
- Lau, K. V., Maher, K., Altiner, D., Kelley, B. M., Kump, L. R., Lehrmann, D. J., et al. (2016). Marine Anoxia and Delayed Earth System Recovery after the End-Permian Extinction. *Proc. Natl. Acad. Sci. USA* 113, 2360–2365. doi:10.1073/pnas.1515080113
- Le Vaillant, M., Barnes, S. J., Mungall, J. E., and Mungall, E. L. (2017). Role of Degassing of the Noril'sk Nickel Deposits in the Permian-Triassic Mass Extinction Event. *Proc. Natl. Acad. Sci. USA* 114, 2485–2490. doi:10.1073/pnas.1611086114
- Li, M., Grasby, S. E., Wang, S.-J., Zhang, X., Wasylenko, L. E., Xu, Y., et al. (2021). Nickel Isotopes Link Siberian Traps Aerosol Particles to the End-Permian Mass Extinction. *Nat. Commun.* 12, 2024. doi:10.1038/s41467-021-22066-7
- Liu, G., Feng, Q., Shen, J., Yu, J., He, W., and Algeo, T. J. (2014). Decline of Siliceous Sponges and Spicule Miniaturization Induced by Marine Productivity Collapse and Expanding Anoxia during the Permian-Triassic Crisis in South China. *PALAIOS* 28, 664–679. doi:10.2110/palo.2013.p13-035r
- McManus, J., Berelson, W. M., Coale, K. H., Johnson, K. S., and Kilgore, T. E. (1997). Phosphorus Regeneration in continental Margin Sediments. *Geochim. Cosmochim. Acta* 61, 2891–2907. doi:10.1016/S0016-7037(97)00138-5
- Meijers, M. J. M., Smith, B., Kirscher, U., Mensink, M., Sosson, M., Rolland, Y., et al. (2015). A Paleolatitude Reconstruction of the South Armenian Block (Lesser Caucasus) for the Late Cretaceous: Constraints on the Tethyan Realm. *Tectonophysics* 644–645, 197–219. doi:10.1016/j.tecto.2015.01.012
- Mora, C., Wei, C. L., Rollo, A., Amaro, T., Baco, A. R., Billett, D., et al. (2013). Biotic and Human Vulnerability to Projected Changes in Ocean Biogeochemistry over the 21st Century. *PLOS Biol.* 11, e1001682. doi:10.1371/journal.pbio.1001682
- Mort, H. P., Adatte, T., Föllmi, K. B., Keller, G., Steinmann, P., Matera, V., et al. (2007). Phosphorus and the Roles of Productivity and Nutrient Recycling during Oceanic Anoxic Event 2. *Geol* 35, 483. doi:10.1130/G23475A.1
- Murphy, J., and Riley, J. P. (1962). A Modified Single Solution Method for the Determination of Phosphate in Natural Waters. *Analytica Chim. Acta* 27, 31–36. doi:10.1016/S0003-2670(00)88444-5
- Newell, N. D. (1967). "Revolutions in the History of Life," in *Geological Society of America Special Paper*. Boulder 89, 63–91. doi:10.1130/SPE89-p63
- Paytan, A., and McLaughlin, K. (2007). The Oceanic Phosphorus Cycle. *Chem. Rev.* 107, 563–576. doi:10.1021/cr0503613
- Penn, J. L., Deutsch, C., Payne, J. L., and Sperling, E. A. (2018). Temperature-dependent Hypoxia Explains Biogeography and Severity of End-Permian marine Mass Extinction. *Science* 362, eaat1327. doi:10.1126/science.aat1327
- Piper, D. Z., and Calvert, S. E. (2009). A marine Biogeochemical Perspective on Black Shale Deposition. *Earth-Science Rev.* 95, 63–96. doi:10.1016/j.earscirev.2009.03.001
- Rampino, M. R., Rodriguez, S., Baransky, E., and Cai, Y. (2017). Global Nickel Anomaly Links Siberian Traps Eruptions and the Latest Permian Mass Extinction. *Sci. Rep.* 7, 12416. doi:10.1038/s41598-017-12759-9
- Raup, D. M., and Sepkoski, J. J. (1982). Mass Extinctions in the Marine Fossil Record. *Science* 215, 1501–1503. doi:10.1126/science.215.4539.1501
- Redfield, A. C., Ketchum, B. H., and Richards, F. A. (1963). The Influence of Organisms on the Composition of Seawater. *The sea* 2, 26–77.
- Reinhard, C. T., Planavsky, N. J., Gill, B. C., Ozaki, K., Robbins, L. J., Lyons, T. W., et al. (2017). Evolution of the Global Phosphorus Cycle. *Nature* 541, 386–389. doi:10.1038/nature20772
- Riccardi, A. L., Arthur, M. A., and Kump, L. R. (2006). Sulfur Isotopic Evidence for Chemocline Upward Excursions during the End-Permian Mass Extinction. *Geochim. Cosmochim. Acta* 70, 5740–5752. doi:10.1016/j.gca.2006.08.005
- Rothman, D. H., Fournier, G. P., French, K. L., Alm, E. J., Boyle, E. A., Cao, C., et al. (2014). Methanogenic Burst in the End-Permian Carbon Cycle. *Proc. Natl. Acad. Sci.* 111, 5462–5467. doi:10.1073/pnas.1318106111
- Roxy, M. K., Modi, A., Murtugudde, R., Valsala, V., Panickal, S., Prasanna Kumar, S., et al. (2016). A Reduction in marine Primary Productivity Driven by Rapid Warming over the Tropical Indian Ocean. *Geophys. Res. Lett.* 43, 826–833. doi:10.1002/2015GL066979
- Ruttenberg, K. C. (1992). Development of a Sequential Extraction Method for Different Forms of Phosphorus in marine Sediments. *Limnol. Oceanogr.* 37, 1460–1482. doi:10.4319/lo.1992.37.7.1460
- Ruttenberg, K. C. (1993). Reassessment of the Oceanic Residence Time of Phosphorus. *Chem. Geology* 107, 405–409. doi:10.1016/0009-2541(93)90220-D
- Schobben, M., Joachimski, M. M., Korn, D., Leda, L., and Korte, C. (2014). Palaeotethys Seawater Temperature Rise and an Intensified Hydrological Cycle Following the End-Permian Mass Extinction. *Gondwana Res.* 26, 675–683. doi:10.1016/j.gr.2013.07.019
- Schobben, M., Foster, W. J., Sleveland, A. R. N., Zuchuat, V., Svendsen, H. H., Planke, S., et al. (2020). A Nutrient Control on marine Anoxia during the End-Permian Mass Extinction. *Nat. Geosci.* 13, 640–646. doi:10.1038/s41561-020-0622-1
- Schoepfer, S. D., Henderson, C. M., Garrison, G. H., and Ward, P. D. (2012). Cessation of a Productive Coastal Upwelling System in the Panthalassic Ocean at the Permian-Triassic Boundary. *Palaeogeogr. Palaeoclimatol. Palaeoecol.* 313–314, 181–188. doi:10.1016/j.palaeo.2011.10.019

- Schoepfer, S. D., Shen, J., Wei, H., Tyson, R. V., Ingall, E., and Algeo, T. J. (2015). Total Organic Carbon, Organic Phosphorus, and Biogenic Barium Fluxes as Proxies for Paleomarine Productivity. *Earth-Sci. Rev.* 149, 23–52. doi:10.1016/j.earscirev.2014.08.017
- Schoepfer, S. D. (2013). Termination of a Continent-Margin Upwelling System at the Permian-Triassic Boundary (Opal Creek, Alberta, Canada). *Glob. Planet. Change* 15, 21–35. doi:10.1016/j.gloplacha.2012.07.005
- Shen, J., Algeo, T. J., Hu, Q., Zhang, N., Zhou, L., Xia, W., et al. (2012). Negative C-Isotope Excursions at the Permian-Triassic Boundary Linked to Volcanism. *Geology* 40, 963–966. doi:10.1130/G33329.1
- Stanley, S. M. (2016). Estimates of the Magnitudes of Major marine Mass Extinctions in Earth History. *Proc. Natl. Acad. Sci. USA* 113, E6325–E6334. doi:10.1073/pnas.1613094113
- Steiner, Z., Lazar, B., Torfstein, A., and Erez, J. (2017). Testing the Utility of Geochemical Proxies for Paleoproductivity in Oxic Sedimentary marine Settings of the Gulf of Aqaba, Red Sea. *Chem. Geol.* 473, 40–49. doi:10.1016/j.chemgeo.2017.10.012
- Sun, Y., Joachimski, M. M., Wignall, P. B., Yan, C., Chen, Y., Jiang, H., et al. (2012). Lethally Hot Temperatures during the Early Triassic Greenhouse. *Science* 338, 366–370. doi:10.1126/science.1224126
- Sun, Y. D., Zulla, M. J., Joachimski, M. M., Bond, D. P. G., Wignall, P. B., Zhang, Z. T., et al. (2019). Ammonium Ocean Following the End-Permian Mass Extinction. *Earth Planet. Sci. Lett.* 518, 211–222. doi:10.1016/j.epsl.2019.04.036
- Sun, Y. D., Richoz, S., Krystyn, L., Grasby, S. E., Chen, Y. L., Banerjee, D., et al. (2021). Integrated Bio-Chemostratigraphy of Lower and Middle Triassic marine Successions at Spiti in the Indian Himalaya: Implications for the Early Triassic Nutrient Crisis. *Glob. Planet. Change* 196, 103363. doi:10.1016/j.gloplacha.2020.103363
- Svensen, H., Planke, S., Polozov, A. G., Schmidbauer, N., Corfu, F., Podladchikov, Y. Y., et al. (2009). Siberian Gas Venting and the End-Permian Environmental Crisis. *Earth Planet. Sci. Lett.* 277, 490–500. doi:10.1016/j.epsl.2008.11.015
- Taylor, S. R., and McLennan, S. M. (1985). *The Continental Crust: Its Composition and Evolution*. 1st ed. Oxford: Blackwell Scientific Publications.
- Trappe, J. (1994). *Pangean Phosphorites - Ordinary Phosphorite Genesis in an Extraordinary World?* Editors Embry, A. F., Beauchamp, B., and Glass, D. J. (Pangea: Global Environments and Resources. Canadian Society of Petroleum Geologists), 469–478.
- Van Cappellen, P., and Ingall, E. D. (1994). Benthic Phosphorus Regeneration, Net Primary Production, and Ocean Anoxia: A Model of the Coupled marine Biogeochemical Cycles of Carbon and Phosphorus. *Paleoceanography* 9, 677–692. doi:10.1029/94PA01455
- Wenchen, X., Ning, Z., Guoqing, W., and Kakuwa, Y. (2004). Pelagic Radiolarian and Conodont Biozonation in the Permo-Triassic Boundary Interval and Correlation to the Meishan GSSP. *Micropaleontology* 50, 27–44. doi:10.1661/0026-2803(2004)050[0027:pracbi]2.0.co;2
- Wignall, P. B., and Hallam, A. (1992). Anoxia as a Cause of the Permian/Triassic Mass Extinction: Facies Evidence from Northern Italy and the Western United States. *Palaeogeogr. Palaeoclimatol. Palaeoecol.* 93, 21–46. doi:10.1016/0031-0182(92)90182-5
- Wignall, P. B., and Twitchett, R. J. (1996). Oceanic Anoxia and the End Permian Mass Extinction. *Science* 272, 1155–1158. doi:10.1126/science.272.5265.1155
- Wignall, P. B., Bond, D. P. G., Grasby, S. E., Pruss, S. B., and Peakall, J. (2020). Controls on the Formation of Microbially Induced Sedimentary Structures and Biotic Recovery in the Lower Triassic of Arctic Canada. *GSA Bull.* 132, 918–930. doi:10.1130/B35229.1
- Yang, S.-C., Kelly, R. L., Bian, X., Conway, T. M., Huang, K.-F., Ho, T.-Y., et al. (2021). Lack of Redox Cycling for Nickel in the Water Column of the Eastern Tropical North Pacific Oxygen Deficient Zone: Insight from Dissolved and Particulate Nickel Isotopes. *Geochim. Cosmochim. Acta* 309, 235–250. doi:10.1016/j.gca.2021.07.004
- Yasuda, N., Miyamoto, N., Fujiwara, Y., Yamamoto, T., and Yusa, Y. (2016). Effects of Food Availability on Growth and Reproduction of the Deep-Sea Pedunculate Barnacle *Heteralepas Canci*. *Deep Sea Res. Oceanogr. Res. Pap.* 108, 53–57. doi:10.1016/j.dsr.2015.12.008
- Zhang, Y., Shi, G. R., He, W.-h., Wu, H.-t., Lei, Y., Zhang, K.-x., et al. (2016). Significant Pre-Mass Extinction Animal Body-Size Changes: Evidences from the Permian-Triassic Boundary Brachiopod Faunas of South China. *Palaeogeogr. Palaeoclimatol. Palaeoecol.* 448, 85–95. doi:10.1016/j.palaeo.2015.11.020
- Zhang, F., Algeo, T. J., Romaniello, S. J., Cui, Y., Zhao, L., Chen, Z.-Q., et al. (2018). Congruent Permian-Triassic $\delta^{238}\text{U}$ Records at Panthalassic and Tethyan Sites: Confirmation of Global-Oceanic Anoxia and Validation of the U-Isotope Paleoredox Proxy. *Geology* 46, 327–330. doi:10.1130/G39695.1

Conflict of Interest: The authors declare that the research was conducted in the absence of any commercial or financial relationships that could be construed as a potential conflict of interest.

Publisher's Note: All claims expressed in this article are solely those of the authors and do not necessarily represent those of their affiliated organizations, or those of the publisher, the editors and the reviewers. Any product that may be evaluated in this article, or claim that may be made by its manufacturer, is not guaranteed or endorsed by the publisher.

Copyright © 2022 Müller, Sun, Yang, Fantasia and Joachimski. This is an open-access article distributed under the terms of the Creative Commons Attribution License (CC BY). The use, distribution or reproduction in other forums is permitted, provided the original author(s) and the copyright owner(s) are credited and that the original publication in this journal is cited, in accordance with accepted academic practice. No use, distribution or reproduction is permitted which does not comply with these terms.